# Recognition of the granular airborne portion in a flighted rotary drum

M. Kozakovic, J. Havlica, L. Le Guen, S. Parez, Florian Huchet

# Recognition of the granular airborne portion in a flighted rotary drum

Kozakovic M.[1, 2], Havlica J.[2, 3], Le Guen L.[4], Parez S.[2, 3], **Huchet F.[4]**

[1] *Jan Evangelista Purkyně University in Ústí nad Labem, Faculty of Mechanical Engineering, Pasteurova 1, 400 96 Ústí nad Labem Czech Republic*

[2] *Jan Evangelista Purkyně University in Ústí nad Labem, Faculty of Science, Pasteurova 3632/15, 400 96 Ústí nad Labem, Czech Republic*

[3] *The Czech Academy of Sciences, Institute of Chemical Process Fundamentals, Rozvojova 2/135, 165 02 Prague, Czech Republic*

[4] *Université Gustave Eiffel, MAST/GPEM, Campus de Nantes, Allée des Ponts et Chaussées CS5004 44344 Bouguenais cedex France*

***corresponding address:*** *florian.huchet@univ-eiffel.fr*

## Highlights

- Granular regimes are identified in a rotary drum composed from 1 to 25 flights.
- Impaired mass transport occurred in an under-loading regime.
- Different methodologies for airborne portion detection are compared.
- Dispersion of the airborne particles is discussed.

## Keywords

Granular Dynamics; Particulates System; Discrete Element Method; Rotary drum

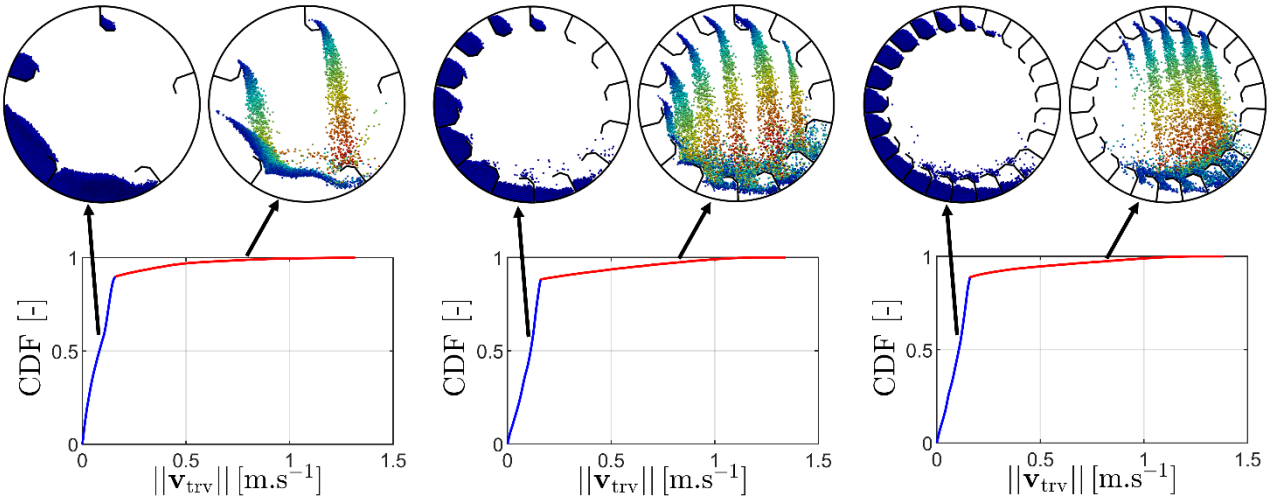



## Abstract

This article deals with numerical simulation via Discrete Element Method (DEM) in a flighted rotary drum with a varying number of flights from 1 to 25 at a constant load of particles. The granular behavior kinematics is studied in the three regimes: under-, design- and over-loading. It was shown that the behavior of granular material during the unloading process from the flights governs the regime transitions. The cross-sectional distribution analysis of the granular material in the different parts of the drum established the existence of two dense media (bed and flights), and one dilute medium (in the airborne portion). Since one of the criteria that affect the efficiency of heat transport between the gas and the particles media is the number of particles in the airborne phase, three recognition methods are proposed to detect the airborne portion. Based on geometry, velocity magnitude, and minimal separation distance, the comparison between them provides a basis for discussion about the relevance of each method in detecting these airborne particles.


## 1. Introduction

The rotary kiln is an industrial facility that covers numerous fields of applications involving heat transfer between a solid load and freeboard gases (Gallo et al., 2019) by convective, conductive, and radiative mechanisms which operate simultaneously (Le Guen et al., 2017) (Seidenbecher et al., 2021). The kinematics of the granular system plays a significant interest in the energy performance process (Tavakkol et al., 2021). Without any baffle, four modes of behavior depending on the drum's rotation speed can arise: avalanching, rolling, cataracting, or centrifuging (Mellmann, 2001). A granular curtain occurs only if a set of baffles are sealed at

the inner drum wall. It promotes a significant airborne portion of the granular medium (Paredes et al., 2017). The airborne portion offers an augmentation of the area of exchange between the freeboard gases and the granular materials compared to the smooth case. The increasing of the active surface area between the granular material and the hot gases media is suited for the heating and drying operations, e.g., sludge drying (Khadija Ettahi et al., 2022) or clinkering calcination (Mungyeko Bisulandu and Huchet, 2022), drying of mineral (Le Guen et al., 2013) or olive stones, (Gómez-de la Cruz et al., 2022). The contribution of the convective and radiative heat exchanges in the airborne portion was recognized as no-negligible for the high-temperature processes (Piton et al., 2015). Even if the conductive transfers into the bed of grains remain generally much less critical than the two others, the conductive processes are nevertheless responsible for regenerative heat exchanges in rotary kiln (Herz et al., 2012), (Hobbs et al., 2022), and made essential for the process modeling. Accordingly, many attempts have been made to characterize the granular motion in the flighted rotary drum. According to (Ajayi and Sheehan, 2012), one can distinguish the over, under, and design loading regimes for which several predictive models were able to be been evaluated (Karali et al., 2015). For any variety of configurations, it is admitted that we can decompose the granular medium in three unequal portions:

- an airborne portion,
- a bed portion,
- a flights portion,

where flights and bed portions behave as granular dense media while the airborne portion behaves as a dilute medium. However, these granular media act simultaneously, which provides a high level of complexity for their characterization compared to other granular systems (Tang et al., 2022) (Barczi et al., 2018).

An accurate evaluation of the mentioned solid mass fractions is required to get a relevant analysis of the kinematics of the granular medium. It has been then possible to compare Discrete Element Method (DEM) and experimental results established in a lab-scale rotary drum (Zhang et al., 2020). Such parameters are also of paramount importance in energy-integrated models (Piton et al., 2015) or Eulerian models (Nascimento et al., 2019). Indeed, the

heat flux densities are a function of the surface of exchanges which can be computed solely from the knowledge of the solid mass fraction.

In that frame, the present paper is aimed to analyze numerically the kinematic of the granular medium into a rotary drum composed of several numbers of flights ranging from 1 to 25. In this work, dry granular material is composed of monodispersed particles transported in the axial direction of the rotary drum. A particular focus is devoted to the airborne portion for which the particle distribution is assessed from different methodologies. Herein, the granular flow regimes and the optimal particle distribution are assessed from DEM.

# 2. Numerical method

## 2. 1. Discrete Element Method (DEM)

DEM is a Lagrangian method typically used for modeling a large number of particles' interaction and provides a good agreement with experimental results (Zhang et al., 2021) (Havlica et al., 2019). The translational motion of each particle is described by Newton's second law in the following equation

$$m_i \frac{\mathrm{d}^2 \mathbf{r}_i}{\mathrm{d}\tau^2} = \sum_{\substack{j=1 \\ j \neq i}}^{N} \mathbf{F}_{ij} + \mathbf{F}_i^{\mathrm{ext}} \qquad (1)$$

and the rotational motion is expressed as

$$I_i \frac{\mathrm{d}\boldsymbol{\omega}_i}{\mathrm{d}\tau} = \sum_{\substack{j=1 \\ j \neq i}}^{N} \mathbf{M}_{ij} \qquad (2)$$

where the subscript $i$ stands for the value for the $i^{th}$ particle, the subscript $ij$ stands for a pairwise collision between the $i^{th}$ and $j^{th}$ particle, $m_i$ is the particle mass, $N$ is the number of particles, $\tau$ is the time, $\mathbf{r}$ is the position vector, $\mathbf{F}_{ij}$ is the collision force, $\mathbf{F}_i^{\mathrm{ext}}$ is the external force, $\mathbf{M}_{ij}$ is the torque acting on the particle, $\boldsymbol{\omega}_i$ is the rotational velocity, and $I_i$ is the moment of inertia. Within second Newton's law, the fundamental forces acting on particles must be considered. Since the granular material is dry and the particles' diameter is larger than 100 μm, only gravitational and collision forces acting on particles are considered (Havlica et al., 2021). The calculation of the collision forces assumes that particles are compressed linearly

during the collision, i.e., any deformation is sufficiently small to be reversible. This soft-sphere approach is expressed by a non-zero overlap

$$\zeta_{ij}^{N} = R_i + R_j - \left\|\mathbf{r}_i - \mathbf{r}_j\right\| > 0 \,, \tag{3}$$

where $R_i, R_j$ are radii of $i^{th}$ and $j^{th}$ particles and $\mathbf{r}_i, \mathbf{r}_j$ their corresponding position vectors. Mutual collision forces and torques between two particles are then defined as follows

$$\mathbf{F}_{ij} = \mathbf{F}_{ij}^{T} + \mathbf{F}_{ij}^{N}\,, \quad \mathbf{M}_{ij} = R_i \mathbf{n}_{ij} \times \mathbf{F}_{ij}^{T}, \qquad \text{if and only if} \;\; \zeta_{ij}^{N} > 0$$

$$\mathbf{F}_{ij} = 0, \qquad \mathbf{M}_{ij} = 0 \qquad \text{if and only if} \;\; \zeta_{ij}^{N} \leq 0 \tag{4}$$

where $\mathbf{F}_{ij}^{T}$ is the tangential collision force, $\mathbf{F}_{ij}^{N}$ is the normal collision force, $R_i$ is the radius of the $i^{th}$ particle, and $\mathbf{n}_{ij}$ is the unit normal vector. The normal force consists of an elastic part, which is a fundamental Hertz's contact, and a dissipative part. Both parts are expressed as

$$\mathbf{F}_{ij}^{N} = K_{ij}^{N} \zeta_{ij}^{N} \mathbf{n}_{ij} - \gamma_{ij}^{N} \Delta \mathbf{v}_{ij}^{N}\,, \tag{5}$$

where $K_{ij}^{N}$ is the elastic constant for a normal contact, $\gamma_{ij}^{N}$is the damping coefficient and $\Delta \mathbf{v}_{ij}^{N}$ is the normal component of the relative velocity between two particles. The tangential force is expressed as

$$\mathbf{F}_{ij}^{T} = K_{ij}^{T} \left\| \int_0^{\tau_c} \Delta \mathbf{v}_{ij}^{T}(\tau) \mathrm{d}\tau \right\| \mathbf{t}_{ij} - \gamma_{ij}^{T} \Delta \mathbf{v}_{ij}^{T}\,, \tag{6}$$

where $K_{ij}^{T}$ is the elastic constant for tangential contact, $\gamma_{ij}^{T}$ is the stiffness coefficient, $\Delta \mathbf{v}_{ij}^{T}$ is the tangential component of relative velocity, $\tau_c$ is the time of particle contact, and $\mathbf{t}_{ij}$ is the unit tangential vector. The tangential force of a particle has no fundamental basis and essentially expresses the surface properties of the material. However, the magnitude of the tangential force is limited by fundamental Coulomb frictional limit

$$\left\|\mathbf{F}_{ij}^{T}\right\| \geq \mu \left\|\mathbf{F}_{ij}^{N}\right\| \;\rightarrow\; \left\|\mathbf{F}_{ij}^{T}\right\| = -\mu \left\|\mathbf{F}_{ij}^{N}\right\| \mathbf{t}_{ij}\,, \tag{7}$$

where μ stands for the coefficient of friction. The equations for Hertzian coefficients used in these equations are listed in Table I.

The dynamics of granular material are governed by a system of second-order differential equations. For their solution, the velocity Verlet algorithm with linear damping is used. Particles' position is computed by the equation

$$\mathbf{r}(\tau + \Delta\tau) = \mathbf{r}(\tau) + \mathbf{v}(\tau)\Delta\tau + \frac{\mathbf{F}(\tau)}{m}\Delta\tau^2 , \tag{8}$$

where $\mathbf{r}$ is the position vector, $\Delta\tau$ is the timestep, $\mathbf{F}(\tau)$ is the force at time $\tau$ and $m$ stand for mass. The velocity is computed as follows

$$\mathbf{v}(\tau + \Delta\tau) = \mathbf{v}(\tau) + \mathbf{v}(\tau)\Delta\tau + \frac{\Delta\tau}{2\,m}[\mathbf{F}(\tau + \Delta\tau) + \mathbf{F}(\tau)] . \tag{9}$$

In the velocity Verlet algorithm only the first power of the time step appears in the relation, which reduces rounding errors. The velocity Verlet algorithm cannot be used for velocity-dependent forces, see the second terms in Eqs. (5) and (6). Therefore, in this case, the force is split into conservative and dissipative parts

$$\mathbf{a}(\mathbf{r}, \mathbf{v}, \tau) = \mathbf{v}(\tau) + \mathbf{v}(\tau)\Delta\tau + \frac{\Delta\tau}{2\,m}(\mathbf{F_{cons}}(\mathbf{r}, \tau) - \mathbf{F_{diss}}(\mathbf{v})) , \tag{10}$$

and in the particular case of linear damping

$$\mathbf{F_{diss}}(\mathbf{v}) = \gamma\,\mathbf{v} \tag{11}$$

is the velocity computed as follows

$$\mathbf{v}(\tau + \Delta\tau) = \frac{1}{1+\frac{\gamma}{2\,m}\Delta\tau}\left[\mathbf{v}(\tau)\left(1 - \frac{\gamma}{2\,m}\Delta\tau\right) + \frac{\Delta\tau}{2\,m}(\mathbf{F}(\tau - \Delta\tau) + \mathbf{F}(\tau))\right] . \tag{12}$$

Table I: The relations of the coefficients used in the collision model for the formulation of normal and tangential forces; $\nu$ is Poisson's ratio, $Y$ is Young's modulus and $e$ is the coefficient of restitution.

| | |
|---|---|
| Damping coefficient | $\gamma_{ij}^{N} = -2\sqrt{\frac{5}{6}}\frac{\log e}{\log^2(\mathrm{e}+\mathrm{n}^2)}\sqrt{2Y_{ij}^{eff}m_{ij}^{eff}\sqrt{R_{ij}^{eff}\zeta^{N_{ij}}}}$ |
| Effective mass and radius | $\frac{1}{m_{ij}^{eff}} = \frac{1}{m_i} + \frac{1}{m_j}; \frac{1}{R_{ij}^{eff}} = \frac{1}{R_i} + \frac{1}{R_j};$ |

| | |
|---|---|
| Effective shear modulus | $\frac{1}{G_{ij}^{eff}} = \frac{2(2+\nu_i)(1-\nu_i)}{G_i} + \frac{2(2+\nu_i)(1-\nu_j)}{G_j}$ |
| Effective Young modulus | $\frac{1}{Y_{ij}^{eff}} = \frac{(1-\nu_i^2)}{Y_i} + \frac{(1-\nu_j^2)}{Y_j}$ |
| Normal elastic constant | $K_{ij}^{N} = \frac{4}{3} Y_{ij}^{eff} \sqrt{R_{ij}^{eff} \zeta^{N_{ij}}}$ |
| Tangential elastic constant | $K_{ij}^{T} = 8\, G_{ij}^{eff} \sqrt{R_{ij}^{eff} \zeta^{N_{ij}}}$ |
| Stiffness coefficient | $\gamma_{ij}^{T} = -2\sqrt{\frac{5}{6}} \frac{\log e}{\log^2(e+n^2)} \sqrt{8\, G_{ij}^{eff} m_{ij}^{eff} \sqrt{R_{ij}^{eff} \zeta^{N_{ij}}}}$ |

## 2. 2. Geometrical and numerical set-up

The scheme of the studied rotary drum is shown in Fig. 1. The length and the diameter of the studied rotating drum were chosen according to (Silveira et al., 2022a).

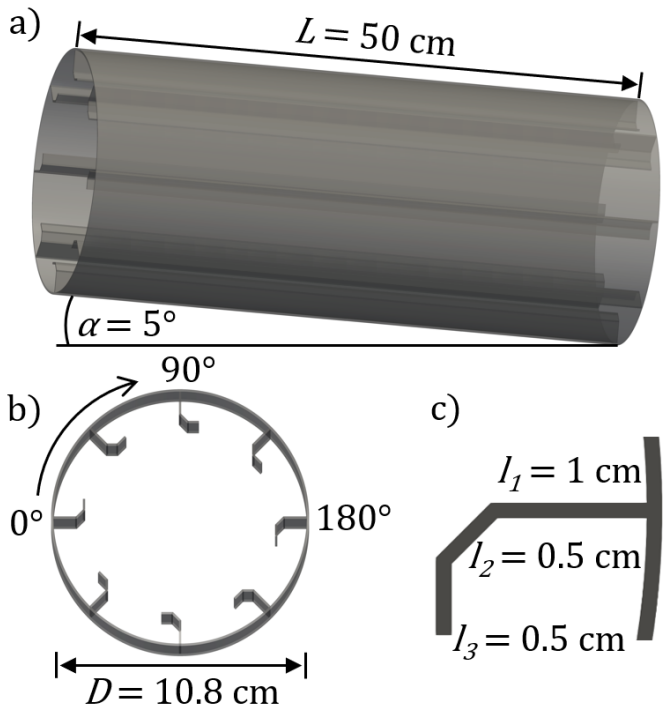

Figure 1: Geometry scheme of the rotary drum: a) side view; b) front view; and c) detail of a flight.

The geometry of the flight was based on previous research presented by (Piton et al., 2015). The overview of the kiln's geometrical parameters is given in Fig.1.

Material and numerical parameters used in DEM simulations are set in Table II. These parameters were chosen according to the previous work of Silveira et al. (Silveira et al., 2022). To study the particles' movement in the flighted rotary drum, the number of flights $N_f$ was varying from 1 to 25 with the constant particles' loading $H$. The upper flights' number is geometrically limited by a steric constrict, i.e., minimum distance between two successive flights is required for particles passage between flights. In order to reduce the computational time, the length of the computational domain is $L_{part} = 5$ cm. Continuous transport of particles in the longitudinal direction of the rotary drum is ensured by using periodic boundary conditions. All the simulations were performed for 20 revolutions to reach the steady state.

Table II: Material and numerical simulation parameters

| Parameters | | | |
|---|---|---|---|
| Symbol | Quantity | Unit | Value |
| $d_p$ | Particle's diameter | [mm] | 1.09 |
| $e_{pp}$ | Coefficient of restitution (particle-particle) | [-] | 0.8 |
| $e_{pw}$ | Coefficient of restitution (particle-wall) | [-] | 0.9 |
| Fr | Froude number | [-] | 0.0274 |
| $L_{part}$ | Rotary drum simulation length | [m] | 0.05 |
| $N$ | Number of particles | [-] | 63,837 |
| $N_f$ | Number of flights | [-] | 1-25 |
| $N_{rev}$ | Number of revolutions | [-] | 20 |
| $V$ | Filling volume ratio | [%] | 15 |
| $Y$ | Young's modulus | [Pa] | $5.10^6$ |
| α | Rotary drum inclination | [deg] | 5 |
| $\mu_{pp}$ | Coefficient of friction (particle-particle) | [-] | 0.7 |

| Parameters | | | |
|---|---|---|---|
| $\mu_{pw}$ | Coefficient of friction (particle-wall) | [-] | 0.4 |
| $\mu_r$ | Coefficient of rolling friction | [-] | 0.04 |
| $\nu$ | Poisson's ratio | [-] | 0.3 |
| $\rho$ | Density of the material | [kg m$^{-3}$] | 2445 |
| $\Delta\tau$ | Timestep | [s] | 2.10$^{-5}$ |
| $\omega$ | Drum rotational speed | [rpm] | 21.3 |

# 3. Results and discussion

In this section, the dynamic behavior of granular particles is analyzed by using global characteristics. The first part describes the loading regimes, and the granular unloading is depicted in one flight. Particles' unloading is supported by the analysis of the kinetic energies. Based on these results, different approaches to airborne portion detection are formulated in the second subsection.

## 3.1 Granular behavior in the cross-sectional area

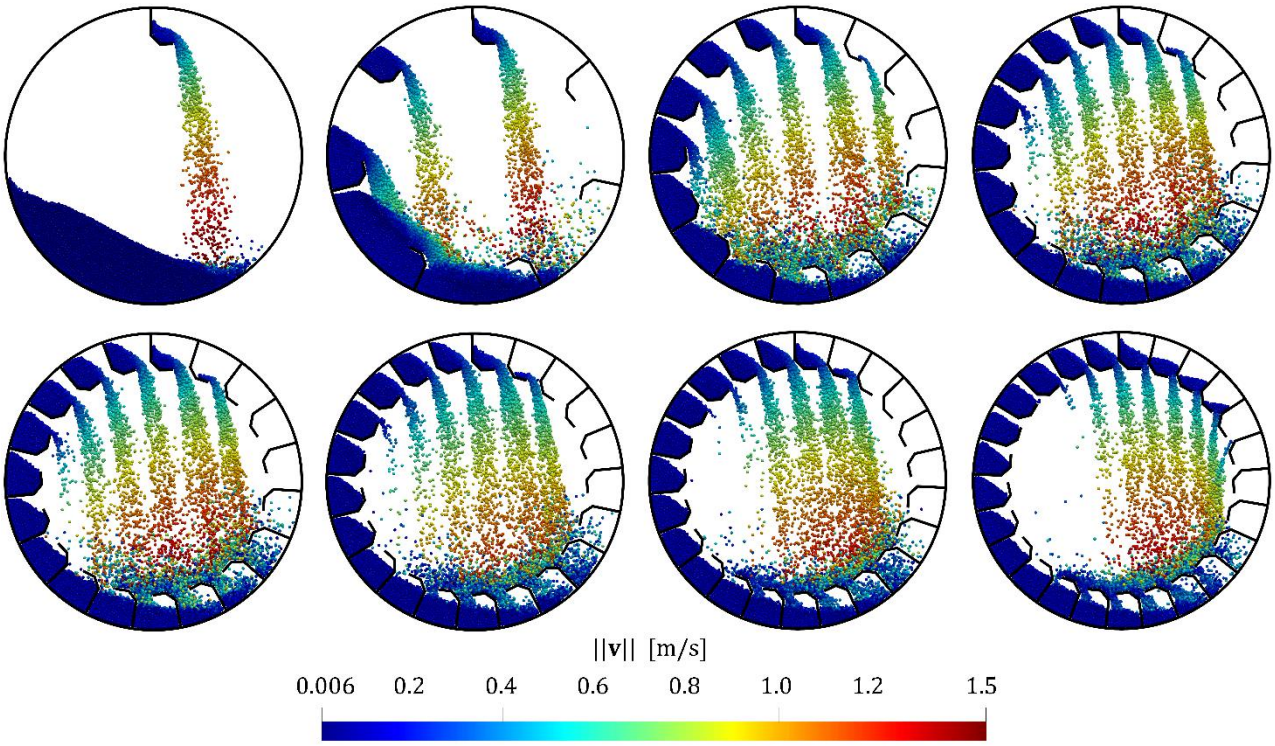


Figure 2: Visualization of particles colored by the magnitude of the velocity in the 20$^{th}$ revolution of the rotary kiln for 1, 7, 11, and 15 flights in the first row and 19, 21, 23, and 25 flights in the second row.

This section analyses the granular dynamic behavior and particles' unloading. In Fig. 2, transverse snapshots of the rotary drum for different numbers of flights are shown. As can be seen from the figure, the number of flights fundamentally affects the behavior of the system and the formation of the airborne phase. As aforementioned, the first snapshot (one flight) shows particles at low-velocity magnitude close to zero located in the flight and the bottom of the drum. A vertical particle's flux is fallen by gravitational acceleration. Accordingly, the holdup (i.e. the volume ratio) can be computed for any portion by using the following relationship

$$H = H_{\mathrm{b}} + H_{\mathrm{fs}} + H_{\mathrm{a}} = \frac{N_{\mathrm{b}}}{N} + \frac{N_{\mathrm{fs}}}{N} + \frac{N_{\mathrm{a}}}{N}, \tag{13}$$

where $H$ is the portion of particles, $N$ is the number of particles, subscript b denotes the particles in the bed, subscript fs in the flights, and subscript a in the airborne.

As the number of flights increases, particles are dropped and form curtains, as generally observed experimentally (LeGuen et al., 2011). However, the shape of these curtains and the number of particles in the airborne portion depend on the number of flights. At the lower number of flights, the lowest coverage of the kiln's central part occurs. For a medium number of flights, a uniform release of particles from flights can be observed in the entire area of the rotary drum. For the highest number of flights, the granular unloading process is non-uniform and a zone without particles arises.

To interpret particles' behavior, the holdup and the holdup difference of particles within the flight are herein analyzed as a function of the angle, see Fig. 3. The angle $\delta = 0°$ is defined according to the position of the first flight as shown in Fig. 1. Since the volume ratio of particles inside the drum is constant, three regimes of granular unloading of flight should occur as the number of flights increases. A regime of over-loading corresponds to a few numbers of flights exhibiting the starting of the granular unloading before reaching an angle equal to zero or $\delta < 0°$. The design-loading regime corresponds to the starting of the granular unloading at the angle, $\delta = 0°$. The under-loading regime corresponds to the starting of the granular unloading at the angle, $\delta > 0°$.

The variation of one flight holdup, $H_{\mathrm{f}}$, as a function of the angle for the studied numbers of cases from 1 to 25 flights is presented in Fig. 3a). From the figure, it is possible to distinguish

the under-loading regime that is characterized by the decline of holdup in the first part of the rotating cycle for the highest number of flights. However, it is difficult to distinguish the over- and design-loading regimes from these results. Indeed, for each of them, the granular unloading is progressively performed for $0° < \delta \lesssim 120°$. Above 120°, the flights are completely emptied.

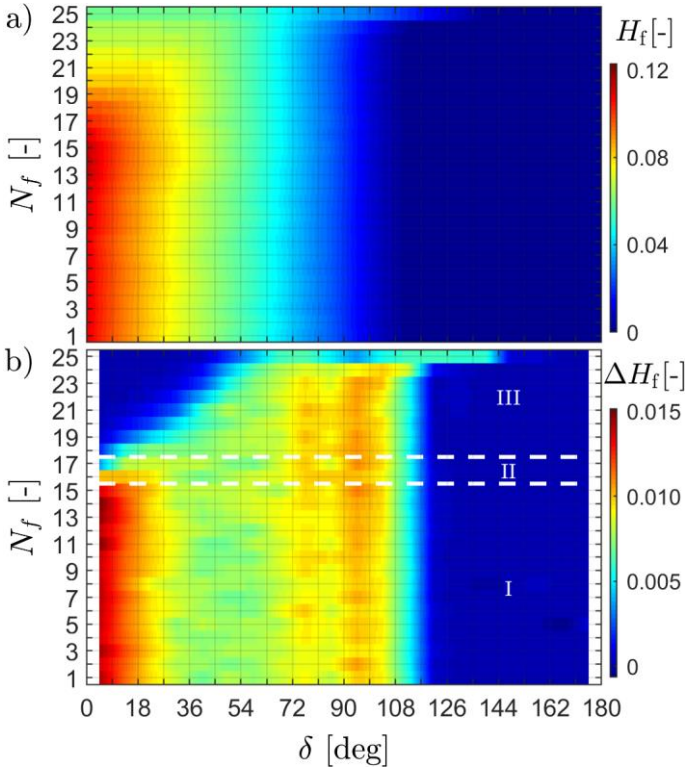


Figure 3: a) The holdup $H_f$ of particles within the flight depending on its angular position for different numbers of flights. b) The holdup difference of particles in the flight depends on its angular position. zone I: over-loading regime; zone II : design-loading regime; zone III : under-loading regime.

Now consider the difference in flight holdups defined as

$$\Delta H_f = H_f(\delta + \Delta\delta) - H_f(\delta), \tag{14}$$

where $\Delta\delta$ stands for the following angular difference of the drum rotation equal to 9°. Variable $\Delta H_f$ corresponds with the physical amount of particles dropped from the flight during displacement of the rotating drum by angle $\Delta\delta$. Obtained results are presented in Fig. 3 b). Based on Fig. 3, one can get the boundaries of each granular unloading regime and we defined them as

- the over-loading regime (I) is reached between 1 and 15 flights;

- the design-loading regime (II) is reached between 16 and 17 flights;

- the under-loading regime (III) is reached between 18 and 25 flights.

In the over-loading regime, particles are steeply discharging out of the flight for an inclination lower than 18°. For inclination between 27° to 63°, the particles are dropped out of the flight at a nearly constant rate. The rest of the flight's load is intensively discharged for an inclination above 72°. This increase in particles unloading is due to particles retention by the $l_3$ segment of the flight's geometry. The flight is completely emptied for an inclination around 120°. The under-loading regime is characterized by a decrease in a holdup in each flight at a zero angle in comparison with other regimes. This decrease in holdup is caused by the redistribution of particles in favor of supplementary flights. Consequently, particles in the flight are unloaded with a delay which increases with the number of flights. The design-loading regime is characterized by almost constant unloading of particles during the inclination of the flight from 18° to 108° compared to over- and under-loading regimes. It can be assumed that this range may have a positive effect on the occurrence of the airborne portion.

Holdup analysis showed a very valuable insight into particles' unloading out of the flight. Particles' distribution within a flighted rotary kiln requires a description of the kinetic behavior of the solid load finely in order to understand the change in regimes of particles' flowing deeply. Considering the cylindrical geometry, the obtained data were transformed from the Cartesian coordinate system ($x,y,z$) into a Cylindrical one ($r,\varphi,z$). To analyze the kinematics of the particles in the system, the individual square components of the average particles' kinetic energies in cylindrical coordinates are assessed. In order to evaluate the kinematic behavior of the system independently on the rotational velocity of the rotary drum, results are plotted in dimensionless values in such a way that

$$E_{k,s}^{*} = \frac{\langle \frac{1}{N}\sum_{j=1}^{N} \frac{1}{2} m v_{s,j}^{2} \rangle}{\frac{1}{2} m {v_p}^2} = \frac{\langle \frac{1}{N}\sum_{j=1}^{N} v_{s,j}^{2} \rangle}{\frac{\pi}{30}\omega_p^2 \frac{D^2}{4}}, \quad s = r, \varphi, z, \tag{15}$$

where $v_{s,j}$ is the $s^{\text{th}}$ component of the velocity vector of the $j^{th}$ particle, $N$ is the number of particles in the drum, $\frac{1}{2} m(\pi \omega_p^2 D^2/120)$ is the kinetic energy of a single particle located on the

wall of the rotary drum moving with the rotational velocity $\omega_p = 21.3$ rpm. Here brackets stand for the average value over the last 5 revolutions of the kiln.

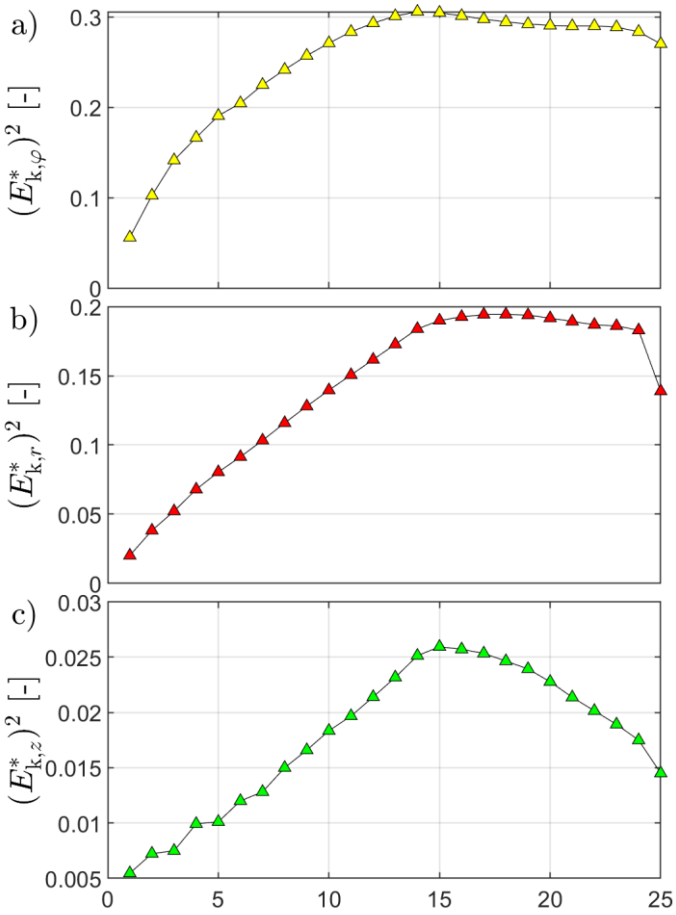


Figure 4: Dimensionless contributions of kinetic energies in cylindrical coordinates depending on the number of flights: a) axial, b) tangential, and c) radial contribution.

The resulting values of dimensionless kinetic energies representing the kinematic behavior of the system are shown in Fig. 4. It can be seen that an increasing number of flights promotes the transport of energy into the system up to a certain critical number of flights. As shown in Fig. 4, the tangential motion dominates in the rotary kiln, and the tangential contribution of kinetic energy $E^*_{k,\varphi}$ always reaches its highest value from all kinetic energy contributions regardless of the number of flights in the system. The radial kinetic energy $E^*_{k,r}$ is the second most important contribution to the overall kinetic energy of particles, and it is about 30 % lower compared to the tangential one. The radial movement represents the motion of the particles in the transverse section governed by the free fall of particles. Assuming that the movement of the granular material is not affected by the surrounding gas, the axial movement of the particles arising mainly due to the rotary drum inclination in the longitudinal direction,

and it is the least significant movement with the lowest kinetic energy, see Fig. 4c). From a qualitative point of view, it can be seen that kinetic energies increase in regime I (over-loading type regime), reach a maximum value in regime II (design-loading type regime), and with slightly decrease $E_{k,\varphi}^{*}$ and $E_{k,r}^{*}$ contributions in regime III (under-loading type regime). In the case of the axial contribution to the total kinetic energy, the decrease in $E_{k,z}^{*}$ in regime III is significant.

By comparing kinetic energies in Fig. 4 with visualizations in Fig. 2, a higher number of flights support the increase of kinetic energy transport in regime I. It is obvious from the visualization that a more significant number of particles are transported from the bed part in the case of more flights in this regime. However, according to one flight's holdup, these particles reach a flow rate that results in a steep unloading out of the flight, see Fig. 3 b). The proposed regime II is characterized by maximum energy transport into the system, and at the same time, particles are uniformly unloaded from the flights during drum rotation. The regime III is characterized by a decrease in the kinetic energy within the drum. In this case, in addition to the fact that the amount of particles in the bed is reduced to the minimum, the flights are already not entirely filled with particles, and the flight's holdup decrease, see Fig. 3 a). In this last regime, because flights contain small amounts of particles, the starting of granular material unloading is delayed, and the uniform distribution of the airborne phase decreases. Since the kinetic energies decrease for the higher number of flights, an impaired mass transport in the system occurs. This phenomenon can have negative impacts on the longitudinal and transverse mass flow in the rotary drum.

## 3. 2. Recognition of the airborne portion

The recognition of the airborne portion in the flighted rotary drum is of significant interest in numerous classes of unit operations, as stated in the introduction. The usual way performs image processing in order to outline the curtain of particles in the central region of the rotary drum (Silveira et al., 2022a) (Zhang et al., 2021). Such methods have been applied in many works, each having developed its own procedure of assessment. The main drawback of this type of method is that it is obeyed to no physical criteria, and does not consider an a priori definition of the airborne portion.

In the present section, three methods are introduced to recognize the airborne portion for comparison's sake:

- The first is based on geometry criteria, as already used for the determination of airborne phase in previous works (Silveira et al., 2022b)
- The second is based on the identification of two granular flow regimes so, called "slow" and "rapid" from a threshold velocity to be determined.
- The third one is related to the minimum separation distance between particles.

Figure 5 shows the determination of the airborne portion via geometry limit. Here, the airborne portion is identified with all particles within a critical distance from the drum's interior defined as the region outside the reach of the flights

$$r_{\mathrm{p}} \leq D/2 - l_1 - l_2 \sin 45° + a \approx 0.042 \text{ m}, \quad (16)$$

where $a = 0.001$ m is the width of the flight. The advantage of this approach is its simple implementation. On the other hand, the geometric approach cannot distinguish between the airborne and the bed phase at the bottom of the rotary kiln, as evident from Fig. 5. Even if there is no bed portion for II and III regimes, see Fig. 5 b) and c), alone particles in flights area are not detected by this method. Therefore, the airborne portion must be determined by another approach especially in regime I.

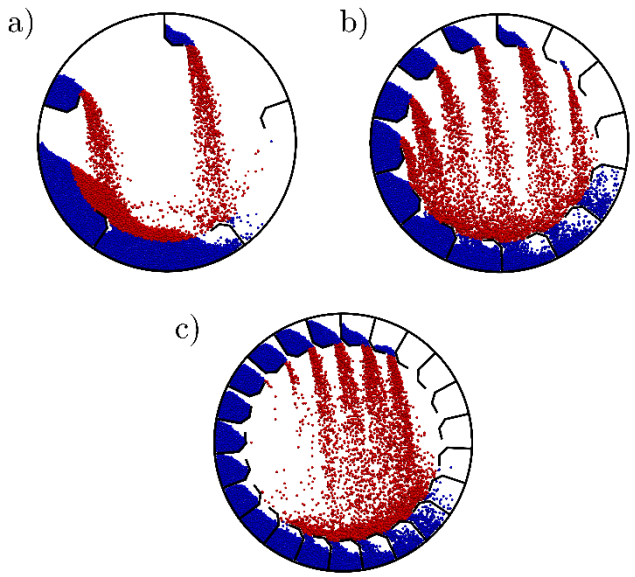


Figure 5: The visualization of the airborne portion via geometry method a) 5, b) 14, and c) 23 flights in the 20th revolution. Red particles form the airborne portion. Blue particles are the passive portion.

The second proposed criterion is based on the following physical phenomenon: particles located in the bed and flights move relatively slower than particles in the airborne portion. The velocity magnitude shown in Fig. 2 supports such consideration for any number of flights. However, a threshold velocity needs to be established in order to identify these two granular flow regimes: "*slow*" and "*rapid*". To determine the threshold value of the transition between these two regimes, it is possible to analyze a cumulative distribution function (CDF):

$$C(\|\mathbf{v}_{\mathrm{trv}}\|) = P\left(\left\|\mathbf{v}_{\mathrm{trv}}^{\mathrm{less}}\right\| \leq \|\mathbf{v}_{\mathrm{trv}}\|\right), \tag{17}$$

where $\mathbf{v}_{\mathrm{trv}}$ is the transverse velocity vector defined as

$$\|\mathbf{v}_{\mathrm{trv}}\| = \sqrt{v_{\varphi}^2 + v_r^2}, \tag{18}$$

The right-side side of Eq. (17) represents the probability that the transverse velocity magnitude of a particle is lower than $\|\mathbf{v}_{\mathrm{trv}}\|$.

The CDF defined by Eq. (17) is shown in Fig. 6. Here, the change between the two parts is based on the significant change in the behavior of the derivative of the CDF according to the magnitude of the transverse velocity. This threshold value is constant and independent of the number of flights, and, for our system, its value is equal to around $0.16\ \mathrm{m.\,s^{-1}}$. Using this threshold value, it is, therefore, possible to identify particles in the airborne portion as all particles with the transverse velocity magnitude

$$\|\mathbf{v}_{\mathrm{trv}}\| \geq \left\|\mathbf{v}_{\mathrm{trv}}^{\mathrm{lim}}\right\| = 0.16\ \mathrm{m.\,s^{-1}}\ . \tag{19}$$

From Fig. 2, it is evident that particles in the passive portion are in close contact, and have a lower velocity magnitude than the detected limit. The particles in the passive portion move with the magnitude of the kiln's velocity of order or slower, and it is less than the limit found by the CDF. As can be seen from Fig. 6, the method still detects the upper fast-moving layers of the bed portion as the airborne phase. In addition, some particles in the airborne phase are miss-identified as passive due to their temporally decreased velocity, for example, after a collision. These are a few individual particles that do not affect the final characterization of the airborne portion.

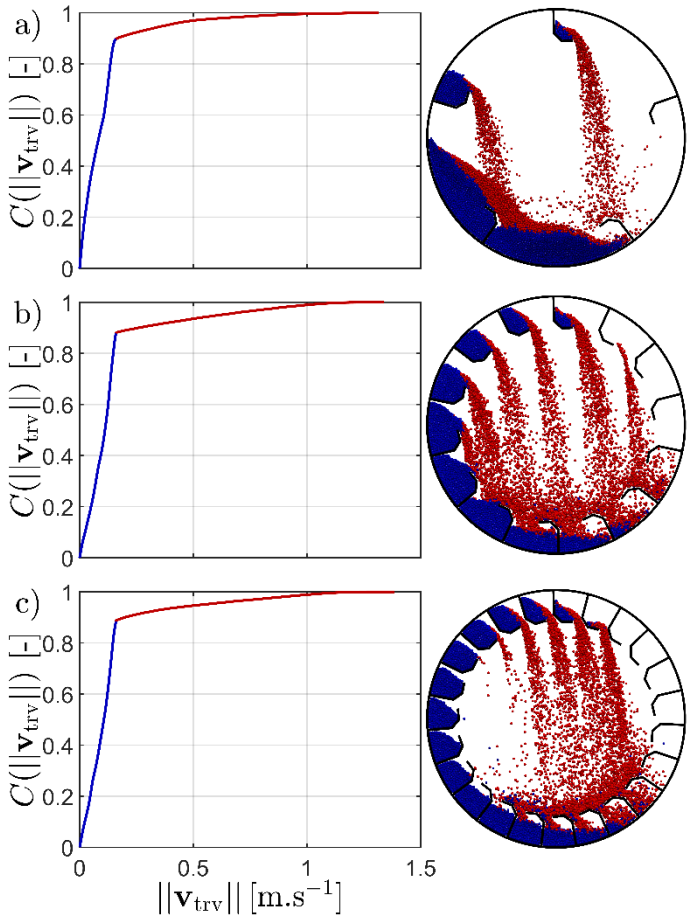


Figure 6: The visualization of the airborne portion (red) and passive portion (blue) by using the method of velocity magnitude threshold for a) 5, b) 14, and c) 23 flights in the 20th revolution. Left column: the dependence of the CDF on the magnitude of transversal velocity. Right column: snapshots of the rotary drum with colored particles according to the phases.

The third proposed method is to define the airborne portion from a critical separation distance between grains. It can be assumed that the particles in the passive phase form a dense granular material with a much higher contact number than the particles located in the passive portion.

A convenient way to describe interparticle distances is via the Radial Distribution Function (RDF). The RDF computes the probability of finding a particle at a certain distance from the reference particle. It provides information on the average interparticle spacing, the coordination number, and the degree of disorder of the material. The RDF is the ratio of the density of particles $\upsilon(r)$ at a distance $r$ from a reference particle to the overall density of particles in the system, $\upsilon$. Since the reference particle is arbitrary, such single-particle distributions are averaged over all particles in the system

$$g(r) = \frac{\langle \upsilon(r) \rangle}{\upsilon}. \tag{20}$$

The RDF is shown in Fig. 7 for different numbers of flights. We observe a significant peak at a distance of around one particle diameter. The position of the peak indicates the first layer of particles around the reference particles and refers to particles that are in direct contact with the reference. This case is typical of the passive portion of the granular system. The RDF then steeply decreases to a second smaller peak, around 2.1 mm. This is the probability of particles located in the second layer around the particle. As can be seen from Fig. 7, with an increasing number of flights, there is a decrease in the value of the first peak in the over-loading regime. This is due to the decreasing amount of particles in the passive phase and the rising number of particles in the airborne phase with higher interparticle distance. The minimum magnitude of the first peak can be observed for the number of flights corresponding to the design-loading regime. In the under-loading regime, a slight increase in RDF can again be observed with an increasing number of flights due to the reduction of the airborne portion.

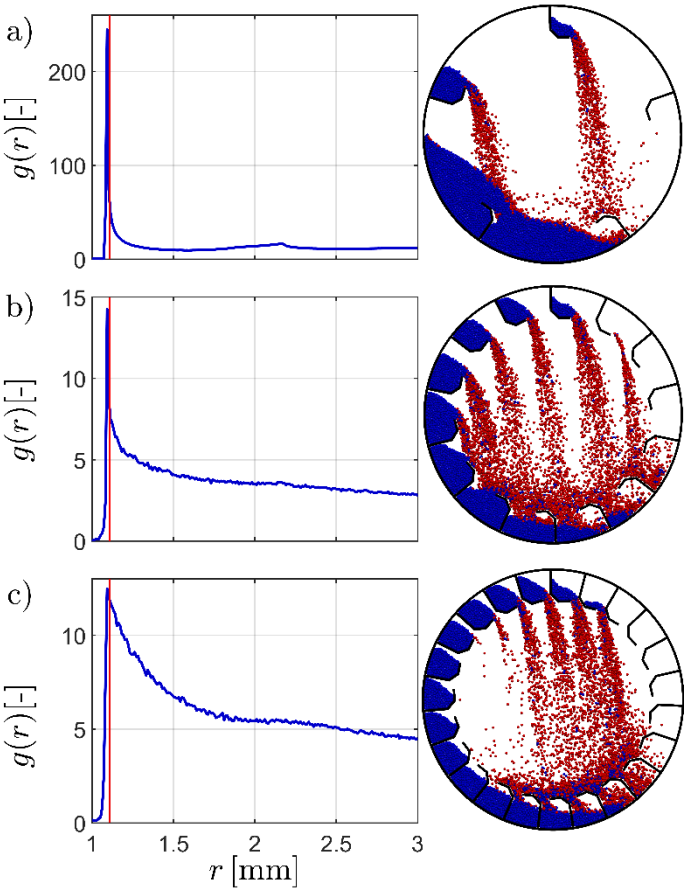


Figure 7: The visualization of the airborne portion (red) and the passive portion (blue) by using the critical separation distance of $1.1d_{\mathrm{p}}$ for a) 5, b) 14, and c) 23 flights in the 20th revolution. Left column: the dependence of the RDF on the distance $r$. Right column: snapshots of the rotary drum with colored particles according to the phases.

Based on the RDF results, it is possible to estimate a threshold of the particle separation distance for the airborne portion detection. The position of the first peak $r = 1d_{\mathrm{p}}$ corresponds to the distance between the closest neighbors in the passive phase. The average separation of particles in the airborne phase should be larger. We, therefore, identify particle $i$ as an airborne particle if it satisfies the following criterion

$$\min\left\|\mathbf{r}_i - \mathbf{r}_j\right\| > R_i + R_j + l_{\mathrm{skin}} \quad . \tag{19}$$

In other words, the minimum distance of an airborne particle from another particle is greater than the close contact distance, $R_i + R_j = d_{\mathrm{p}}$, extended by a skin length, $l_{skin}$. In Fig. 7, the identification of airborne particles is shown for a critical separation of 1.1 $d_{\mathrm{p}}$, corresponding to $l_{\mathrm{skin}}$=0.1 $d_{\mathrm{p}}$. This critical separation distance is shown in the left panel by the red line. Visualizing the particles in the airborne portion using the critical separation distance (right

column) shows that the number of detected particles is slightly lower in regime I than by the velocity limit method because, unlike the velocity criterion, particles in the bed are detected more correctly. In regimes II and III, the estimation of the airborne phase by all methods is almost identical.

A comparison of all three approaches to airborne portion identification is presented in Fig. 8. In the case of the critical separation distance, the identification of the airborne portion is dependent on the $l_{\mathrm{skin}}$ parameter. Fig 8 presents the variability of the airborne portion results for the three selected different distances $l_{\mathrm{skin}}$ which give rise to some significant changes in the identification of the airborne particles when the value of $l_{\mathrm{skin}}$ varies. Based on the comparison with the other methods, the interparticle distance, $l_{\mathrm{skin}} = 0.1\ d_{\mathrm{p}}$, is suited in our studied case. However, the high sensitivity of the predicted airborne portion on the critical separation distance limits the practical usefulness of this criterion of recognition of the airborne portion. Therefore, further, its utilization will require deeper analysis.

Fig. 8 also shows that the airborne portion detected by geometric criterion is overestimated compared to the velocity and critical separation distance thresholds for the over-loading regime I. This inaccuracy is caused by a rough assumption that the central region of the rotary kiln is fully covered by the airborne portion. This simple assumption misleadingly includes particles in the bed. Therefore, the number of particles detected in the airborne portion is several times higher in the case of the geometric criterion compared to the detection of particles by the velocity and separation distance criteria. Moreover, a difference between the airborne portion detected by velocity and separation distance occurs in regime I. Indeed, the velocity-based detection method identifies the upper, fast-moving particles in the bed portion as the airborne phase. As a result, this method overestimates the airborne portion as well, although not as much as the geometrical method. In the design-loading regime II and in the under-loading regime III, the recognition of the airborne portion by all three methods are in good agreement.

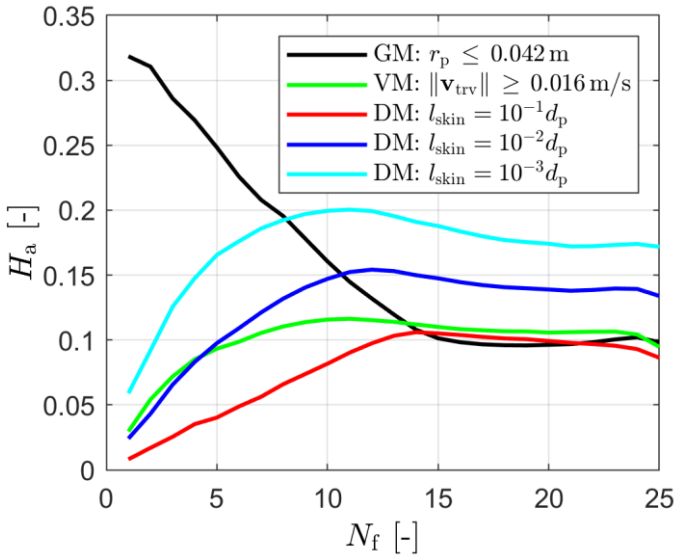


Figure 8: The holdup of airborne portion depending on the number of flights detected by three methods: (GM) the geometry method, (VM) the velocity method, and (DM) the minimum separation distance method for three different $l_{\mathrm{skin}}$.

The airborne portion holdup $H_a$ depending on the angular position of the kiln is plotted in Fig. 9 for all three methods and the whole range of flight numbers. For the over-loading regime I, the airborne particles are nonuniformly distributed, especially for less than 5 flights. The granular materials develop an airborne portion in a limited angular position, while large "dead" zones arise with almost no particles identified in the central region of the drum.

As shown in Figs. 8 and 9, the geometry-based method overestimates the airborne portion in the over-loading regime I. The two others methods show similar trends with a quantitative difference due to the different ways of evaluating the bed portion at the bottom of the device.

A permanent regime is reached in term of airborne portion, manifested by uniform (angle-independent) granular unloading. It occurs from 14 flights corresponding approximatively to the design-loading regime II. It can also be noticed that the velocity-based and separation distance-based methods provide the maximum overall airborne portion in the design-loading regime II. For the under-loading regime III, the airborne portion decreases slightly or is almost constant with increasing flights number depending on the detection method.

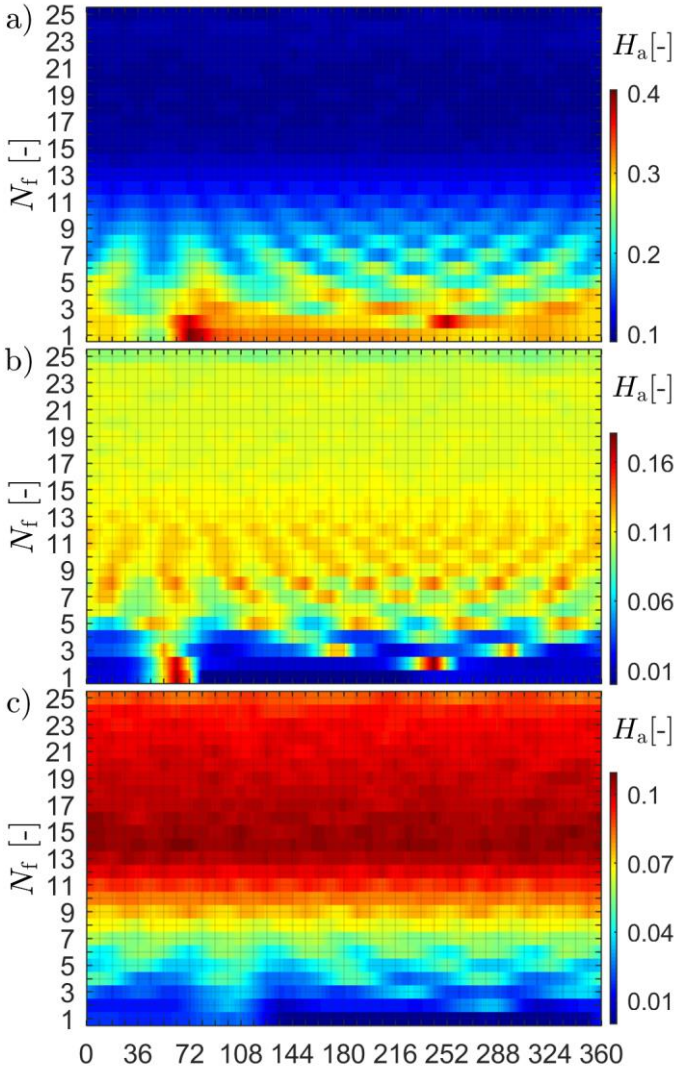


Figure 9: Holdup of the airborne particles during their granular unloading for the overall studied flight numbers: a) the geometry method, b) the velocity method, and c) the minimum separation distance method.

# 4. Conclusions

The analysis of the granular behavior of a rotary drum composed of different numbers of flights, from 1 to 25, is herein numerically performed at constant load via DEM. Since the load was set to constant volume fraction, the over-, design- and under-loading regimes were able to be characterized according to the flight increment. One fundamental question that we are seeking in that paper is to better understand how is performed the granular load distribution in the cross-sectional area for any loading regimes. As noted in the literature, it has also been observed that flights influence this distribution and break down this granular load into three

parts: i) bed, ii) flights and iii) airborne, the second and especially the third portion is intended to be explored herein in detail.

The characterization of the loading regimes depends on the granular unloading kinematics into the flight. The design regime was tracked here in a thin range of the number of flights (between 16 and 17 flights). It was found out that the design-loading regime is characterized by relatively constant unloading of particles out of the flight, which promotes the occurrence of a homogenous airborne portion. Moreover, the kinetic energy of loaded particles in transverse and longitudinal directions reached its highest peak for the design-loading regime. At this point, the most kinetic energy from the rotary drum is transported in the load.

The recognition of the airborne portion has been extensively studied by proposing two methods, the velocity magnitude, and the minimum separation distance, to compare to a standard geometry approach. This latter is based on the selection of boundaries of the airborne area according to visual characteristics. The velocity magnitude was able to distinguish the slow and fast-moving particles. The minimal separation distance criteria were able to distinguish the minimal nearest neighbors' distance in the most immediate neighborhood of the particle and based on this information, determine the dense and dilute phases of the granular material. Since different quantification approaches were able to be computed, the work has allowed us to make an estimation of their range of validity. The geometric approach appears to be unreliable, especially in an over-loaded regime while it is quite reliable for the two others. Moreover, the airborne portion estimation from velocity magnitude and minimum separation distance thresholds seems to be more accurate for any loading regimes.

To conclude, the recognition of the three granular portions composed of dense and dilute regimes appears quite tricky if we are seeking to characterize them from one physical criterion. Some drawbacks have been shown in any method; some captured airborne particles should be normally considered in one of the two dense regimes, bed and flights respectively, or few captured particles in the dense regimes should be considered in the airborne portion. Anyway, since the velocity threshold is based on the principle that the velocity magnitude of the airborne portion is governed by the gravitational acceleration; such method is well adapted for engineering design. On the other hand, the minimum separation distance threshold supported by the spatial analysis is based on the idea of empty vicinity around the airborne portion. Even if this approach is based on a priori knowledge, and is not supported by a fundamental basis at this time, it opens research questions (such as how to define this

airborne portion rigorously) and engineering studies (such as varying the loading rate, the number of flights and the size of the drum).

## Nomenclature

**List of used variables:**

| | | |
|---|---|---|
| $a$ | Width of the flight | [m] |
| $C$ | Cumulative function | [-] |
| $d$ | Diameter | [m] |
| $D$ | Diameter of the kiln | [m] |
| $e$ | Coefficient of restitution | [-] |
| $E$ | Dimensionless kinetic energy | [-] |
| $\mathbf{F}$ | Force | [N] |
| Fr | Froude number | [-] |
| $g(R)$ | Radial distribution function | [-] |
| $G$ | Shear modulus | [Pa] |
| $H$ | Holdup | [-] |
| $I$ | Moment of inertia | [kg m$^2$] |
| $K$ | Elastic constant | [N m$^{-1}$] |
| $l$ | Length | [m] |
| $L$ | Length of the kiln | [m] |
| $m$ | Mass | [kg] |
| $\mathbf{M}$ | Torque | [N m] |
| $\mathbf{n}$ | Unit normal vector | [-] |
| $N$ | Number | [-] |
| $P$ | Probability function | [-] |
| $\mathbf{r}$ | Position vector, radial coordinate | [m] |
| $R$ | Radius | [mm] |
| $\mathbf{t}$ | Unit tangential vector | [-] |
| $\mathbf{v}$ | Velocity | [m s$^{-1}$] |
| $V$ | Filling volume ratio | [-] |
| $x$ | Coordinate | [m] |
| $z$ | Coordinate | [m] |
| $Y$ | Young's modulus | [Pa] |
| $z$ | Axial coordinate | [m] |
| $\alpha$ | Longitudinal inclination | [deg] |
| $\gamma$ | Stiffness coefficient | [N m$^{-1}$] |
| $\delta$ | Angular position of the flight | [deg] |
| $\Delta\delta$ | Following angular step | [deg] |

| | | |
|---|---|---|
| $\Delta H$ | Holdup difference | [-] |
| $\Delta\tau$ | Timestep | [s] |
| $\zeta$ | Overlap | [m] |
| $\mu$ | Friction coefficient | [-] |
| $\nu$ | Poisson's ratio | [-] |
| $\rho$ | Density of the material | [kg m$^{-3}$] |
| $\tau$ | Time | [s] |
| $\upsilon$ | Number density of particles | [-] |
| $\varphi$ | Tangential coordinate | [deg] |
| $\omega$ | Rotational velocity | [rpm] |

**List of sub- and supper-scripts:**

| | |
|---|---|
| a | Airborne |
| b | Bed |
| c | Center |
| cons | Conservative |
| d | Drum |
| diss | Dissipative |
| eff | Effective |
| ext | External |
| f | Flight |
| fs | Flights |
| *i* | Value of i$^{th}$ particle |
| *j* | Value of j$^{th}$ particle |
| *ij* | Between i$^{th}$ and j$^{th}$ particles |
| *k* | Kinetic |
| *less* | Less value |
| N | Normal |
| p | Particle |
| part | Part of the drum length in the simulation area |
| pp | Particle-particle interaction |
| pw | Particle-wall interaction |
| rev | Revolution |
| *s* | Index of s$^{th}$ polar coordinate |
| skin | Neighbor skin distance |
| trv | Transversal |
| T | Tangential |
| 1, 2, 3 | Flight's geometry parts |
| * | Nondimensional |

**List of abbreviations:**

| | |
|---|---|
| CDF | Cumulative Distribution function |
| DEM | Discrete Element Method |
| RDF | Radial Distribution Function |

## Acknowledgment

The authors thank the Research Programme Strategy AV21 Water for life for valuable support. Jaromir Havlica and Martin Kozakovic acknowledge the support of this work by the Internal Grant Agency of Jan Evangelista Purkyně University in Ústí nad Labem (project no. UJEP-SGS-2020-53-003-3). Stanislav Parez acknowledges the support of Grant No. 19-21114Y from the Czech Science Foundation (GA CR). This research was supported by the project U21-High Quality of HR for International Area Strengthening II CZ.02.2.69/0.0/0.0/18_053/0017815.

## Reference

Ajayi, O.O., Sheehan, M.E., 2012. Design loading of free flowing and cohesive solids in flighted rotary dryers. Chem Eng Sci 73, 400–411. https://doi.org/10.1016/j.ces.2012.01.033

Barczi, T., Kohout, M., Kozakovic, M., Havlica, J., Ratnayake, C., 2018. Discrete Element Method Simulation and Experimental Validation of Pattern Development in a Rotating Drum Mixer. Chem Eng Technol 41, 1524–1530. https://doi.org/10.1002/ceat.201700607

Gallo, A., Alonso, E., Pérez-Rábago, C., Fuentealba, E., Roldán, M.I., 2019. A lab-scale rotary kiln for thermal treatment of particulate materials under high concentrated solar radiation: Experimental assessment and transient numerical modeling. Solar Energy 188, 1013–1030. https://doi.org/10.1016/j.solener.2019.07.006

Gómez-de la Cruz, F.J., Palomar-Torres, A., Palomar-Carnicero, J.M., Cruz-Peragón, F., 2022. Energy and exergy analysis during drying in rotary dryers from finite control volumes: Applications to the drying of olive stone. Appl Therm Eng 200. https://doi.org/10.1016/j.applthermaleng.2021.117699

Havlica, J., Jirounkova, K., Travnickova, T., Stanovsky, P., Petrus, P., Kohout, M., 2019. Granular dynamics in a vertical bladed mixer: Secondary flow patterns. Powder Technol 344, 79–88. https://doi.org/10.1016/j.powtec.2018.11.094

Havlica, J., Kozakovic, M., Kramolis, D., Travnickova, T., Kohout, M., 2021. The effect of primary and secondary flows on the homogenization process in a vertical bladed mixer. Powder Technol 391, 253–266. https://doi.org/10.1016/j.powtec.2021.06.015

Herz, F., Mitov, I., Specht, E., Stanev, R., 2012. Experimental study of the contact heat transfer coefficient between the covered wall and solid bed in rotary drums. Chem Eng Sci 82, 312–318. https://doi.org/10.1016/j.ces.2012.07.042

Hobbs, A.M., Ooi, J.Y., Adepu, M., Emady, H., 2022. Experimental validation of a particle-based method for heat transfer incorporating interstitial gas conduction in dense granular flow using a rotary drum. Advanced Powder Technology 33, 103426. https://doi.org/10.1016/j.apt.2022.103426

Karali, M.A., Sunkara, K.R., Herz, F., Specht, E., 2015. Experimental analysis of a flighted rotary drum to assess the optimum loading. Chem Eng Sci 138, 772–779. https://doi.org/10.1016/j.ces.2015.09.004

Khadija Ettahi, Meriem Chaanaoui, Vaudreuil Sébastien, Souad Abderafi, Tijani Bounahmidi, 2022. Modeling and Design of a Solar Rotary Dryer Bench Test for Phosphate Sludge. Modelling and Simulation in Engineering 1–11.

Le Guen, L., Huchet, F., Dumoulin, J., Baudru, Y., Tamagny, P., 2013. Convective heat transfer analysis in aggregates rotary drum reactor. Appl Therm Eng 54, 131–139. https://doi.org/10.1016/j.applthermaleng.2013.01.025

Le Guen, L., Piton, M., Hénaut, Q., Huchet, F., Richard, P., 2017. Heat convection and radiation in flighted rotary kilns: A minimal model. Canadian Journal of Chemical Engineering 95, 100–110. https://doi.org/10.1002/cjce.22659

LeGuen, L., Huchet, F., Tamagny, P., 2011. Drying and heating modelling of granular flow: Application to the mix-asphalt processes. Journal of Applied Fluid Mechanics 4, 71–80. https://doi.org/10.36884/jafm.4.03.11936

Mellmann, J., 2001. The transverse motion of solids in rotating cylinders-forms of motion and transition behavior. Powder Technol 118, 251–270. https://doi.org/10.1016/S0032-5910(00)00402-2

Mungyeko Bisulandu, J.R., Huchet, F., 2022. Rotary kiln process: An overview of physical mechanisms, models and applications. Appl Therm Eng 119637. https://doi.org/10.1016/j.applthermaleng.2022.119637

Nascimento, S.M., Lima, R.M., Brandão, R.J., Duarte, C.R., Barrozo, M.A.S., 2019. Eulerian study of flights discharge in a rotating drum. Can J Chem Eng 97, 477–484. https://doi.org/10.1002/cjce.23291

Paredes, I.J., Yohannes, B., Emady, H., Glasser, B.J., Borghard, W.G., Muzzio, F., Cuitiño, A.M., Beeckman, J., Ilias, S., Podsiadlo, P., Jezek, E., Baumgartner, J., 2017. The effect of operating conditions on the residence time distribution and axial dispersion coefficient of a cohesive powder in a rotary kiln. Chem Eng Sci 158, 50–57. https://doi.org/10.1016/j.ces.2016.09.028

Piton, M., Huchet, F., Le Corre, O., Le Guen, L., Cazacliu, B., 2015. A coupled thermal-granular model in flights rotary kiln: Industrial validation and process design. Appl Therm Eng 75, 1011–1021. https://doi.org/10.1016/j.applthermaleng.2014.10.052

Seidenbecher, J., Herz, F., Meitzner, C., Specht, E., Wirtz, S., Scherer, V., Liu, X., 2021. Temperature analysis in flighted rotary drums and the influence of operating parameters. Chem Eng Sci 229, 115972. https://doi.org/10.1016/j.ces.2020.115972

Silveira, J.C., Lima, R.M., Brandao, R.J., Duarte, C.R., Barrozo, M.A.S., 2022a. A study of the design and arrangement of flights in a rotary drum. Powder Technol 395, 195–206. https://doi.org/10.1016/j.powtec.2021.09.043

Silveira, J.C., Lima, R.M., Brandao, R.J., Duarte, C.R., Barrozo, M.A.S., 2022b. A study of the design and arrangement of flights in a rotary drum. Powder Technol 395, 195–206. https://doi.org/10.1016/j.powtec.2021.09.043

Tang, X., Yue, Y., Wang, S., Shen, Y., 2022. Modelling of gas-solid-liquid flow and particle mixing in a rotary drum. Powder Technol 409, 117758. https://doi.org/10.1016/j.powtec.2022.117758

Tavakkol, S., Zirwes, T., Denev, J.A., Jamshidi, F., Weber, N., Bockhorn, H., Trimis, D., 2021. An Eulerian-Lagrangian method for wet biomass carbonization in rotary kiln reactors.

Renewable and Sustainable Energy Reviews 139, 110582. https://doi.org/10.1016/j.rser.2020.110582

Zhang, L., Jiang, Z., Mellmann, J., Weigler, F., Herz, F., Bück, A., Tsotsas, E., 2021. Influence of the number of flights on the dilute phase ratio in flighted rotating drums by PTV measurements and DEM simulations. Particuology 56, 171–182. https://doi.org/10.1016/j.partic.2020.09.010

Zhang, L., Jiang, Z., Weigler, F., Herz, F., Mellmann, J., Tsotsas, E., 2020. PTV measurement and DEM simulation of the particle motion in a flighted rotating drum. Powder Technol 363, 23–37. https://doi.org/10.1016/j.powtec.2019.12.035